Journal of Mechanisms and Robotics

Characterization of spatial parasitic motions of compliant mechanisms induced by manufacturing errors

Zhiwei, Zhu
State Key Laboratory of Ultra-precision Machining Technology, Department of Industrial and System Engineering, The Hong Kong Polytechnic University, Kowloon, Hong Kong SAR, China
wsjdzzw-jx@163.com

Suet, To [a,b] [1]
a. State Key Laboratory of Ultra-precision Machining Technology, Department of Industrial and System Engineering, The Hong Kong Polytechnic University, Kowloon, Hong Kong SAR, China
b. Shenzhen Research Institute of the Hong Kong Polytechnic University, Shenzhen, PR China
sandy.to@polyu.edu.hk

Xiaoqin, Zhou
School of Mechanical Science and Engineering, Jilin University, Changchun 130022, China
xqzhou@jlu.edu.cn

Rongqi, Wang
School of Mechanical Science and Engineering, Jilin University, Changchun 130022, China
gzzjwrq@163.com

Xu, Zhang
School of Mechanical Science and Engineering, Jilin University, Changchun 130022, China
zhangxu8613@163.com

ABSTRACT

This paper proposes a theoretical model for characterizing manufacturing error induced spatial parasitic motions (MESPM) of compliant mechanisms, and investigates the inherent statistic features of MESPM using Monte Carlo simulation. It also applies and extends a novel finite beam based matrix modeling method to theoretically derive the elastic deformation behavior of an imperfect flexural linkage (IFL), which is a basic element of a wide spectrum of compliant mechanisms. A case study of a well-known double parallelogram compliant mechanism (DPCM) is also conducted, and

[1] All correspondence concerning this paper should be addressed to: sandy.to@polyu.edu.hk (S. To)

The following publication Zhu, Z., To, S., Zhou, X., Wang, R., and Zhang, X. (August 18, 2015). "Characterization of Spatial Parasitic Motions of Compliant Mechanisms Induced by Manufacturing Errors." ASME. J. Mechanisms Robotics. February 2016; 8(1): 011018 is available at https://doi.org/10.1115/1.4030586.

the practical parasitic motions of a prototype DPCM are characterized by laser interferometer based measurements.

ABBREVIATIONS

MESPM:	manufacturing error induced spatial parasitic motions
CM:	compliant mechanisms
DPCM:	double parallelogram compliant mechanism
AFM:	atomic force microscope
DOF:	degree-of-freedom
RCFH:	right circular flexure hinge
WEDM:	wire electric discharge machining
IFL:	imperfect flexural linkage
FBMM:	finite beam based matrix modeling
FEA:	finite element analysis
PMU:	parasitic motion uncertainty
SPMU:	sensitivity of the PMU
LSFH:	leaf-spring flexure hinge
CTM:	compliance transformation matrix

NOMENCLATURES

o-xyz:	global coordinate system of the perfect linkage
o^{L}-$x^{L}y^{L}z^{L}$:	global coordinate system of the IFL
$o_k^{\delta} - x_k^{\delta} y_k^{\delta} z_k^{\delta}$:	local coordinate system of the *k*-th pieced beam element
$o_i=(x_i,y_i)$, i=1,2,3,4:	center coordinate of the *i*-th circle
$x_{\min}$ and $x_{\max}$:	position boundary of the IFL along the x-axis

δx_i, i=1,2,3,4:	position deviation of the i-th circle center along the x-axis
R:	nominal radius of the circle
δR_i, i=1,2,3,4:	radius deviation of the i-th circle
α_U and α_L:	inclination angles of the upper and lower curve of the linkage
N:	the number of pieced beam elements
w_k, k=1,2,…N:	width of the k-th beam element
L *and* l:	length of the IFL and beam element
b:	thickness of the IFL
$\mathbf{C}_k^{\delta}$:	compliance matrix of the k-th beam element
$C_{\theta_x,M_x}^{(k)}$:	torsion compliance of the k-th beam element
$\mathbf{C}^{\mathrm{IFL}}$:	compliance matrix of the IFL
$\mathbf{C}^{\mathrm{DPCM}}$:	compliance matrix of the DPCM
E:	modulus of elasticity
G:	modulus of rigidity
μ:	Poisson ratio
α_s:	shear coefficient
z_k, k=1,2,…N:	thickness-to-width ratio of the k-th beam element
$\mathbf{T}_k$, k=1,2,…N:	CTM of the k-th beam element
$\mathbf{T}_i^{\mathrm{L}}$, i=1,2,3,4:	CTM of the i-th IFL
$\mathbf{R}_k$, k=1,2,…N:	rotation matrix of the k-th beam element
$\mathbf{r}_k$, k=1,2,…N:	position vector of the k-th beam element
$\mathbf{S}_k(\cdot)$, k=1,2,…N:	skew-symmetric operator for the k-th beam element
ϕ_i, i=1,2,3,4:	rotation angle of the i-th IFL

$\mathbf{u}$:	motion vector of the DPCM
$\mathbf{F}_{ext}$:	actuation force on the DPCM
ζ :	sensitivity of SPMU along the working direction
χ :	practical parasitic motion along the *z*-axis
ϑ :	practical working motion
k^{δ} and k^{θ}:	proportionality coefficients of the translation and pitch errors
L_1 and L_2:	distances from output to the pitch axis and interferometer

1. INTRODUCTION

Compliant mechanisms (CM), serving as the basic precision elements, have been widely employed in micro-/nanomachining, micro-/nanomanipulating, micro-/nanopositioning for surface measurements, and nano-indentation and nano-scratch for material tests [1-4]. In these scenarios, spatial positioning with nano-metric accuracy is crucial to obtain reliable results. For instance, in the atomic force microscope (AFM), the cross-talk between each moving axis of the stage for nano-positioning of samples will cause strong image artifacts [3, 5]. In the nano-indentation, the slight tilt error of the indentation axis will lead to a relatively large deviation of the estimated hardness and modulus [6, 7], and the parasitic motion induced lateral forces and deflections will also significantly affect the testing results, especially for high bandwidth tests [8, 9]. Also, for CM with displacement amplification, local parasitic motions will be amplified along the chain, further deteriorating the system's working performance [10, 11].

In view of mechanical structure of CM, the inherent parasitic motions are mainly derived from the structure design (intrinsic) [12-14] and the manufacturing error induced structure distortions (extrinsic) [15-17]. Generally, the intrinsic parasitic motion can be

diminished by adopting proper structure configuration and elaborated calibrations [13, 18]. On the other hand, significant extrinsic parasitic motion can be induced by manufacturing errors even in very stiff systems [19]. For instance, a theoretical coupling motion of 0.03% could be as much as 1.5% for a practical system attributing to inevitable manufacturing errors [2]. However, it is very difficult for CM with less than six degree-of-freedoms (6-DOF) to compensate for these inevitable spatial parasitic motions caused by manufacturing errors [20]. To diminish the extrinsic parasitic motion, an efficient solution is to select robust parameters for CM during the design process, making it insensitive to manufacturing errors [21, 22]. This process will be highly dependent on the understanding of the relationship between manufacturing tolerance and parasitic motion of CM with any given structure parameters. Motivated by this, Patil et al. investigated manufacturing error induced spatial parasitic motions (MESPM) of a one DOF translation stage based on the screw theory [22]. Ryu and Gweon studied MESPM of a typical compound linear spring by analyzing compliance variations of the common right circular flexure hinge (RCFH) [23]. In the analysis, dominant features of the RCFH were treated as perfect, and the corresponding structure distortion effect was described by adopting another equivalent RCFH with only position, orientation and parameter deviations. However, the treatment was over simplified and the effect of linkage distortion on the parasitic motion was ignored. Following the identified manufacturing error sources, Hwang et al. employed the Taguchi design of experiments to get a robust design of a XYθ stage with complex configuration based on finite element analysis (FEA) [11]. It required repetitive FEA simulations to get the final result and provided an unclear relationship between the parasitic motion and structure parameters. Huh et al.

investigated MESPM of a XY stage from the statistical point of view, the MESPM were also estimated by means of FEA [24]. Attention was focused on the length variations of the connecting leaf springs induced by assembly errors. Similarly, this kind of structural deviation of a compliant constant-force slider crank mechanism has been analytically investigated [25]. However, the FEA based evaluations are often computationally heavy, and the analyses in the two aforementioned studies are also over simplified and far from generalizable.

Practically, the manufacturing error would induce strongly distorted structure shapes, which are far from the regular profiles of the existing flexure hinges as reported. Accordingly, the elastic deformation behavior of the resulting distorted hinges can no longer be finely described by the compliance matrix of the perfect hinges. Besides, it will be more meaningful to describe the parasitic motions in a statistical manner due to the intrinsic uncertainties of manufacturing processes. Motivated by this, a more universal and comprehensive method is proposed in this paper to characterize MESPM. Taking the popular double parallelogram compliant mechanism (DPCM) for instance, MESPM in the complete spatial directions are comprehensively investigated. This research provides guidance for precision engineers and researchers to: (i) analytically characterize spatial parasitic motions of imperfect CM induced by manufacturing errors; (ii) comprehensively understand the dependence of parasitic motion features on structure parameters and manufacturing uncertainties; and (iii) select robust structure parameters and proper manufacturing tolerances to minimize potential parasitic motions.

2. MODELING OF THE IMPERFECT FLEXURAL LINKAGE

A typical flexural linkage involving two RCFHs and a linkage beam, which is a basic element of a wide spectrum of commonly used compliant mechanisms, is illustrated in Fig. 1 [1-3]: *o-xy* is the global coordinate system of the linkage, and $o_i=(x_i,y_i)$ denotes the center of the *i*-th circle in the coordinate. Although various sorts of flexure hinges have been introduced and studied over the last two decades, the most popular RCFH is adopted here as a case study. The proposed method is suitable for all types of flexure hinges.

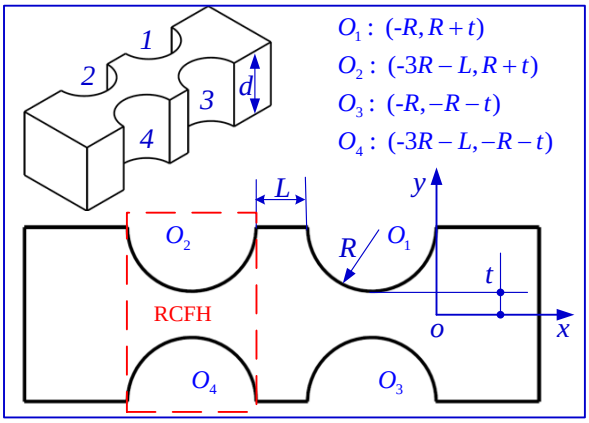

Fig. 1 Schematic of a typical flexural linkage

2.1 Geometry characterization of the imperfect linkage

Wire electric discharge machining (WEDM*)* with multiple steps is a very popular method for fabricating CM [1-3, 23]. However, due to the inconsistency in each step and the moving errors of the WEDM machines, structural errors in CM are inevitable. Herein, the main sources of errors are identified as: a) positioning error of WEDM; b) straightness error of the motions of WEDM; and c) perpendicularity error between the wire and the surface in clamping. To model the resulting geometry of the linkage, the following assumptions are adopted:

a) The fluctuation of the feeding motion of the wire in WEDM only induces compliance variations of the linkage. Instead, the linear error of the feeding contributes more to the parasitic motion of the mechanism. Thus, the wire is assumed to feed straightly and the relative fluctuation is ignored to simplify the modeling.

b) Positioning error of the wire in the WEDM changes the shape of the notch, probably resulting in non-circular or even irregular profiles. The resulting varied compliance can be equivalently obtained by adopting circular profiles of the notch with varied radius [11, 23]. Thus, the distortion of the semi-circles will be approximately treated as semi-circles with equivalent radius in modeling.

c) Perpendicularity error results in the "Parallelism Error" and strongly induce out-of-plane parasitic errors [16, 23]. To simplify the modeling process, the cross sections is approximately treated as rectangles with equivalent rotations as adopted in Refs. [17] and [23].

To describe the geometry of the imperfect flexural linkage (IFL), the perfect linkage is employed as the basis. The radii of the four circles of the IFL are described by the nominal radius R with each deviation δR_i. Position deviations of the centers of the four semi-circles along the x-direction are characterized by 4 independent values δx_i. Straightness error induced inclination of the linkage beam is characterized by α_U and α_L with respect to the lower and the upper curves of the IFL, respectively. Deviations of the centers of the four circles along the y-direction are jointly determined by the inclined lines and the x positions of the centers. The perpendicularity error caused skew effect of

the IFL is ignored when modeling the IFL, while it is equivalently modeled when forming a compliant mechanism. This is detailed in the next section.

The lower or the upper curve of the linkage can be regarded as a combination of three segmented geometric features, namely a tilt line and two circles, with different radiuses connected by the line. Thus, two piece-wise functions are adopted here to respectively describe the upper and lower curves:

$$S^{\mathrm{U}}: y^{\mathrm{U}}=\begin{cases}-\sqrt{\Delta R_1^{\,2}-\left(x-\Delta x_1\right)^2}+y_1+\tan\alpha_{\mathrm{u}}\left(x-\dfrac{x_1+x_2}{2}\right), x\in\left[\Delta x_1-\Delta R_1, \Delta x_1+\Delta R_1\right] \\ \dfrac{y_1+y_2}{2}+\tan\alpha_{\mathrm{u}}\left(x-\dfrac{x_1+x_2}{2}\right), x\in\left[\Delta x_2+\Delta R_2, \Delta x_1-\Delta R_1\right] \\ -\sqrt{\Delta R_2^{\,2}-\left(x-\Delta x_2\right)^2}+y_2+\tan\alpha_{\mathrm{u}}\left(x-\dfrac{x_1+x_2}{2}\right), x\in\left[\Delta x_2-\Delta R_2, \Delta x_2+\Delta R_2\right]\end{cases} \tag{1}$$

$$S^{\mathrm{L}}: y^{\mathrm{L}}=\begin{cases}\sqrt{\Delta R_3^{\,2}-\left(x-\Delta x_3\right)^2}+y_3+\tan\alpha_{\mathrm{L}}\left(x-\dfrac{x_3+x_4}{2}\right), x\in\left[\Delta x_3-\Delta R_3, \Delta x_3+\Delta R_3\right] \\ \dfrac{y_3+y_4}{2}+\tan\alpha_{\mathrm{L}}\left(x-\dfrac{x_3+x_4}{2}\right), x\in\left[\Delta x_4+\Delta R_4, \Delta x_3-\Delta R_3\right] \\ \sqrt{\Delta R_4^{\,2}-\left(x-\Delta x_4\right)^2}+y_4+\tan\alpha_{\mathrm{L}}\left(x-\dfrac{x_3+x_4}{2}\right), x\in\left[\Delta x_4-\Delta R_4, \Delta x_4+\Delta R_4\right]\end{cases} \tag{2}$$

where $\Delta x_i=x_i+\delta x_i$ and$\Delta R_i=R+\delta R_i$, denoting the real x-coordinates of the centers and the equivalent radiuses of the semi-circles. To make the structure physically meaningful, the following constraints for the parameters should be satisfied:

$$\begin{cases}\left|R+\delta R_i\right|>0 \\ x_1+\delta x_1-\left(R+\delta R_1\right)\cos\alpha_{\mathrm{U}}>x_2+\delta x_2+\left(R+\delta R_2\right)\cos\alpha_{\mathrm{U}} \\ x_3+\delta x_3-\left(R+\delta R_3\right)\cos\alpha_{\mathrm{L}}>x_4+\delta x_4+\left(R+\delta R_4\right)\cos\alpha_{\mathrm{L}}\end{cases} \tag{3}$$

From the shadow part as shown in Fig. 2, this part of the IFL features much larger cross sections connecting with the base. It serves rather the base than the flexure hinge and has little contribution to elastic deformations of the IFL. With this concern, the boundary constraints of the IFL can be accordingly determined by:

$$x \in \left[x_{\min}, x_{\max}\right] = \left[\max(\Delta x_2 - \Delta R_2, \Delta x_4 - \Delta R_4), \min(\Delta x_1 - \Delta R_1, \Delta x_3 - \Delta R_3)\right] \quad (4)$$

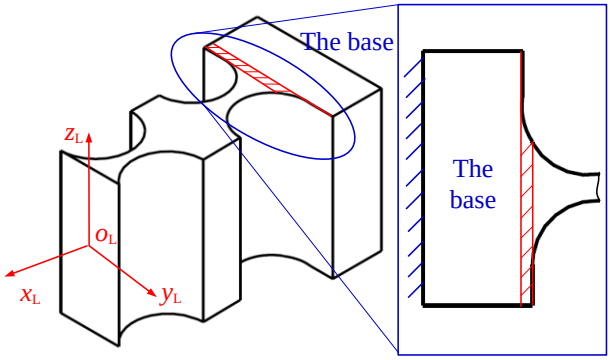

Fig. 2 Structure characteristic of the IFL

2.2 Complete compliance modeling of the IFL

Based on the established models shown in Eq. 1 and Eq. 2, the shapes of the perfect and the imperfect linkages are illustrated in Fig. 3. As the figure shows, the manufacturing error induced structure distortion can be obviously observed, and it can no longer be treated as any existing flexure hinge. Generally, it is potential for the Euler–Bernoulli beam theory based calculus methods, which are popular for obtaining the complete compliance of flexure hinges with various shapes, to obtain the compliance of the IFL [26-28]. However, these methods are not efficient due to the fact that each term of the complete compliance matrix needs to be separately executed by laborious integral operations over the entire flexure length in the modeling. In this paper, a novel finite beam based matrix modeling (FBMM) method which was proposed for typical flexure hinges [29, 30] is adopted and extended to numerically obtain the elastic deformation behavior of the IFLs with any complicated shape. The FBMM requires no prior-knowledge of beam theory or even of calculus, thereby greatly extending the potential applications of the proposed analysis method [29].

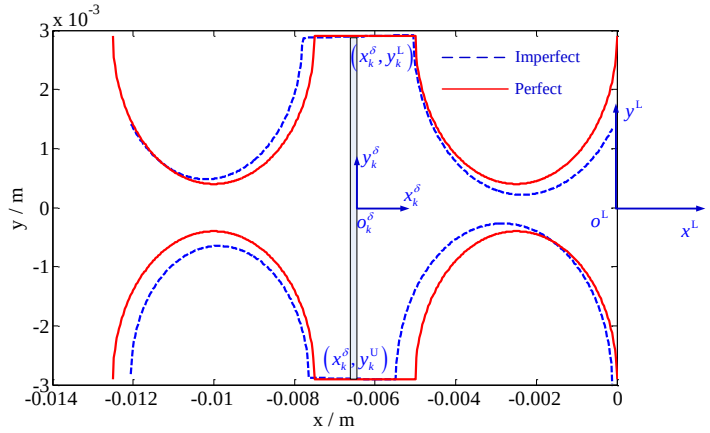

Fig. 3 Schematic of the linkages derived from the mathematical model

In the FBMM process, the IFL is treated as a whole flexural beam and divided into N equal pieces with rectangular cross-sections. Each pieced beam element is operated as a conventional leaf-spring flexure hinge (LSFH) [29]. As shown in Fig. 2, o^L-x^Ly^L denotes the global coordinate of the IFL, and $o_k^\delta - x_k^\delta y_k^\delta$ denotes the local coordinate of the k-th pieced beam element. The position of the k-th beam element in the global coordinate can be expressed by:

$$o_k^\delta = (x_k^\delta, \frac{y_k^L + y_k^U}{2}) \tag{5}$$

where y_k^L and y_k^U will be derived from Eqns. (1) and (2) based on the x_k^δ.

Besides, the equivalent dominant parameters, namely the width w_k, and the length l, of the k-th piece beam can be determined by:

$$\begin{cases} w_k = y_k^L + y_k^U \\ l = \dfrac{x_{\max} - x_{\min}}{N} \end{cases} \tag{6}$$

where N is the number of pieced beam elements.

As discussed above, the pieced beam element is the basic element that can be described by the well-established compliance matrix for LSFHs in terms of small

deformations. To enhance the modeling accuracy, a modified version for the compliance matrix of the *k*-th beam element considering the shearing and torsion behavior is derived by [22]:

$$\mathbf{C}_k^{\ \delta} = \begin{bmatrix} \frac{l}{Ebw_k} & 0 & 0 & 0 & 0 & 0 \\ 0 & \frac{4l^3}{Ebw_k^3}+\frac{\alpha_s l}{Gbw_k} & 0 & 0 & 0 & \frac{6l^2}{Ebw_k^3} \\ 0 & 0 & \frac{4l^3}{Eb^3w_k}+\frac{\alpha_s l}{Gbw_k} & 0 & -\frac{6l^2}{Eb^3w_k} & 0 \\ 0 & 0 & 0 & C^{(k)}_{\theta_x,M_x} & 0 & 0 \\ 0 & 0 & -\frac{6l^2}{Eb^3w_k} & 0 & \frac{12l}{Eb^3w_k} & 0 \\ 0 & \frac{6l^2}{Ebw_k^3} & 0 & 0 & 0 & \frac{12l}{Ebw_k^3} \end{bmatrix} \tag{7}$$

where E and G are the modulus of elasticity and the modulus of rigidity, respectively, b denotes the thickness of the linkage, and α_s is the shear coefficient of the material. With μ being the Poisson ratio, the shear coefficient α_s introduced by Cowper for LSFH is employed [31]:

$$\alpha_s = \frac{12+11\mu}{10(1+\mu)} \tag{8}$$

With the description of torsion behavior of the beam element, most of the existing models mainly depend on the relative magnitude of the cross-section thickness and width, which may be position-varying for variable cross-section hinges (e.g. the RCFH, and the tapered beam) [32, 33]. To accurately describe the torsion for the IFL, a newly developed torsion compliance, which is thickness-to-width ratio independent, is employed with the definition of the ratio $z_k=b/w_k$ [32]:

$$C^{(k)}_{\theta_x,M_x} = \frac{7l}{2G}\left(\frac{1}{w_k b^{\,3}}+\frac{1}{w_k^{\,3} b}\right)\frac{z_k^{\,2}+2.609z_k+1}{1.17z_k^{\,2}+2.191z_k+1.17} \tag{9}$$

Overall, with the assumption that the effects of stress distributions on elastic deformations of flexure hinges can be ignored, the IFL will be regarded as series connections of all the beam elements. Based on the matrix based modeling principle, the compliance of the IFL in the global coordinate can be expressed by [34]:

$$\mathbf{C}^{\mathrm{IFL}} = \sum_{k=1}^{N} \mathbf{T}_k \mathbf{C}_k^{\delta} \mathbf{T}_k^{\mathrm{T}} \tag{10}$$

where $\mathbf{T}_k$ denotes the compliance transformation matrix (CTM), taking on the following form [2, 33-35]:

$$\mathbf{T}_k = \begin{bmatrix} \mathbf{R}_k & \mathbf{S}_k(\mathbf{r}_k)\mathbf{R}_k \\ \mathbf{O} & \mathbf{R}_k \end{bmatrix} \tag{11}$$

where $\mathbf{R}_k$ is the rotation matrix of the local coordinate o_i-$x_iy_iz_i$ with respect to the global coordinate, here, the rotation matrix equals to $\mathbf{I}$. $\mathbf{r}_k$ is the position vector of the point o_i expressed in the global coordinate. $\mathbf{S}_k(\mathbf{r}_k)$ represents the skew-symmetric operator for the vector $\mathbf{r}_k=[x_k,y_k,z_k]$ with the notation:

$$\mathbf{S}_k = \begin{bmatrix} 0 & 0 & \dfrac{y_k^{\mathrm{L}} + y_k^{\mathrm{U}}}{2} \\ 0 & 0 & -(x_{\min} + kl) \\ -\dfrac{y_k^{\mathrm{L}} + y_k^{\mathrm{U}}}{2} & x_{\min} + kl & 0 \end{bmatrix} \tag{12}$$

2.3 Finite element validation of the FBMM

To investigate the efficiency and accuracy of the developed model for characterizing the elastic deformation behavior of the IFL, the commercial FEA software ANSYS is adopted for the estimation of the ‘real’ compliance terms. The material of the IFL in FEA calculation is spring steel 65Mn, the material properties and basic structure parameters of which are given in Table 1. Totally two cases are investigated to demonstrate the effectiveness of the FBMM, and the structural deviations caused by

manufacturing errors are presented in Table 2. Both the FEA and the analytical results are given in Table 3. Taking the FEA results as the benchmark, the relative errors of the FBMM results for the three cases are almost all within 10%, except for the term $\delta z / F_z$, demonstrating the reliability of the FBMM method for further analysis of the distorted CM. The relative large errors of the mentioned term may be caused by the constrained warping and the residual stresses effects [36, 37]. It is suggested that further refinements of the beam theory should be conducted to correct these errors [37].

Table 1. Basic parameters of the IFL

E / GPa	μ	R / mm	t / mm	L / mm	b / mm	N
2.00	0.3	2.5	0.4	2.5	10	1000

Table 2. Deviations of the parameters (/ mm)

	δR_1	δR_2	δR_3	δR_4	δx_1	δx_2	δx_3	δx_4	δb	α_U	α_L
C1	0.2	0.1	-0.15	0.08	-0.12	0.1	0.2	-0.1	0.8	2°	0.4°
C2	-0.1	0.15	0.08	-0.12	0.2	-0.15	0.1	-0.2	-0.5	-1°	0.8°

Table 3. FEA and FBMM results (In SI units)

		$\delta x / F_x$	$\delta y / F_y$	$\delta y / M_z$	$\delta\theta_z / M_z$	$\delta\theta_z / F_y$
C1	FEA	4.82×10^{-9}	5.84×10^{-6}	6.08×10^{-4}	7.20×10^{-2}	5.99×10^{-4}
	FBMM	4.71×10^{-9}	5.47×10^{-6}	5.67×10^{-4}	6.71×10^{-2}	5.67×10^{-4}
	Error	2.28%	6.33%	6.74%	6.81%	5.34%
C2	FEA	4.62×10^{-9}	1.74×10^{-6}	2.15×10^{-4}	4.25×10^{-2}	2.21×10^{-4}
	FBMM	4.56×10^{-9}	1.72×10^{-6}	2.17×10^{-4}	4.28×10^{-2}	2.17×10^{-4}
	Error	1.30%	1.15%	0.93%	0.71%	1.81%
		$\delta z / M_y$	$\delta z / M_x$	$\delta x / M_z$	$\delta z / F_z$	
C1	FEA	2.73×10^{-6}	4.16×10^{-6}	6.69×10^{-6}	4.60×10^{-8}	
	FBMM	2.87×10^{-6}	4.30×10^{-6}	6.19×10^{-6}	3.86×10^{-8}	
	Error	5.12%	3.36%	7.47%	16.08%	
C2	FEA	3.51×10^{-6}	2.43×10^{-7}	3.85×10^{-7}	4.49×10^{-8}	
	FBMM	3.20×10^{-6}	2.58×10^{-7}	3.72×10^{-7}	4.00×10^{-8}	
	Error	8.80%	6.17%	3.37%	10.91%	

3. CHARACTERISTICS OF MESPM OF A NANO-POSITIONING STAGE

A typical DPCM consisting of four flexural linkages is illustrated in Fig. 4. It has been widely implemented in micro-/nano technologies for motion guidance of the actuators [1-3]. Thus, it is adopted herein as a case study to characterize the features of MESPM.

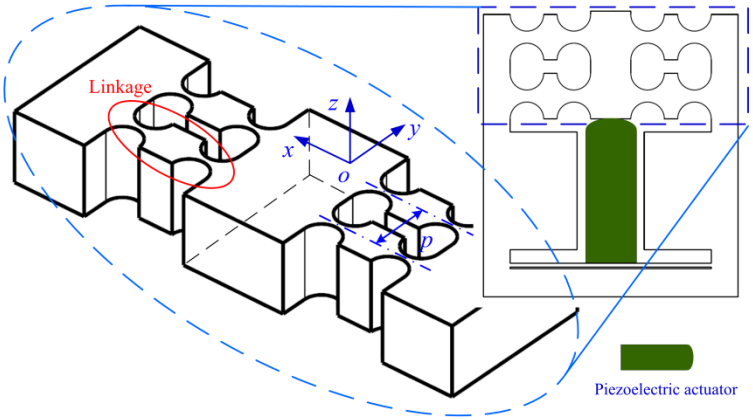

Fig. 4 A typical DPCM

3.1 Modeling the imperfect DPCM

The DPCM with manufacturing error induced structure distortions can be regarded as a holder supported by four parallel IFLs. Thus, following the well-known matrix based compliance modeling method [12, 34], the compliance at the point *o* in the global coordinate can be determined by:

$$\mathbf{C}^{\mathrm{DPCM}} = \left[\sum_{i=1}^{4} \left[\mathbf{T}_i^{\mathrm{L}} \mathbf{C}_i^{\mathrm{IFL}} \left(\mathbf{T}_i^{\mathrm{L}} \right)^{\mathrm{T}} \right]^{-1} \right]^{-1} \tag{13}$$

where $\mathbf{T}_i^{\mathrm{L}}$ denotes the CTM from the local coordinate of the *i*-th IFL to the global coordinate *o-xyz*, which takes the same definition of that in Eq. 11.

As discussed in section 2.1, the perpendicularity error induced skew effects are herein treated as the rotations of the IFL around the *x*-axis with equivalent rotation angles ϕ_i in term of the *i*-th IFL. Thus, the rotation matrix of the *i*-th IFL is determined by

$$\mathbf{R}_i(\phi_i) = \begin{bmatrix} \cos\phi_i & 0 & \sin\phi_i \\ 0 & 1 & 0 \\ -\sin\phi_i & 0 & \cos\phi_i \end{bmatrix} \tag{14}$$

Following the Hook's law, motions of the distorted DPCM can be expressed by:

$$\mathbf{u} = \mathbf{C}^{\mathrm{DPCM}}\mathrm{F}_{\mathrm{ext}} \tag{15}$$

Where **u** denotes the motion vector, and $\mathbf{F}_{\mathrm{ext}}$ denotes the external actuation forces.

3.2 Monte Carlo simulation

Since there are totally around 50 variables of the structure parameters and the compliances are of high nonlinearity with respect to these variables, it is hard to adopt the conventional analysis method to characterize the inherent features of MESPM. Thus, the Monte Carlo simulation is carried out to comprehensively investigate the MEPMs from the statistical point of view. To construct the simulation, we assume that (i) since the mechanism is monolithic and fabricated by one WEDM machine, the manufacturing deviations are treated in the same level; (ii) the parameter deviations are of Gaussian distributions with zero means [17, 24], and (iii) the parameter deviations are mutually independent [17, 24].

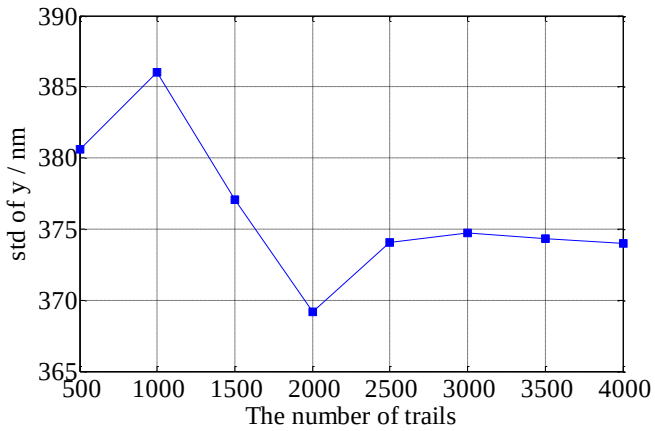

Fig. 5 Variations of the std of deformations in the *y*-axis direction

A precision machining process is assumed to have been used to obtain the mechanism, the variances of δR_i, δx_i and δb are set as 25 μm, and the variances of α_U, α_L and φ_i are set as 0.2^o. The simulations are conducted with 100N actuation forces along the working direction, namely the *y*-axis. To get a reliable number of simulation trials, a set of simulations with different number of trials are conducted, resulting in the standard deviations (Std) of the deformation along the working direction with respect to the number of trials shown in Fig. 5. As illustrated in Fig. 5, when the number of trials reaches 2500, the Std of the corresponding deformation almost converges to a stable level. Thus, the number of the trials is chosen as 3000 in the following analyses. The first four moments of the obtained results, namely, the mean value, the standard deviation, the skewness, and the kurtosis, are utilized to characterize the statistics of the elastic deformation behavior of the imperfect DPCM. The Std denotes the parasitic motion uncertainty (PMU) in the direction, while the skewness and the kurtosis are the measure of the asymmetry and the peakedness of the probability distribution of the parasitic motions, respectively.

Generally, parasitic errors are deviations from working motions. Features of parasitic motions are definitely linked with the desired ones. To fairly compare the

dependences of parasitic motions on structure parameters and manufacturing uncertainties, the sensitivity of spatial parasitic motion uncertainty (SPMU) is defined by:

$$\zeta = \frac{\mathrm{std}(p_i)}{\bar{p}_y} \tag{15}$$

where std(p_i) denotes Std of the deflections in the i-th direction when the mechanism is driven by a 100N force in the y-axis direction, suggesting uncertainty of the corresponding parasitic motion. $\bar{p}_y$ denotes the mean value of the working deflection in the y-axis direction.

3.3 Results and discussion

3.3.1 Effects of structure parameters

There are four fundamental parameters governing the working behavior of the DPCM, namely R, t, b and L. It is crucial to derive a guidance law for choosing these parameters and accordingly achieving the robust design of the mechanism. Thus, the sensitivities of the parasitic motions to the four parameters are investigated based on the designed Monte Carlo simulations. In each simulation, the evaluated parameter will vary within a specified range, while the other three parameters will be set as the constants shown in Table 1 in section 2.3. The obtained PMUs and the SPMUs are illustrated in Fig. 6 below.

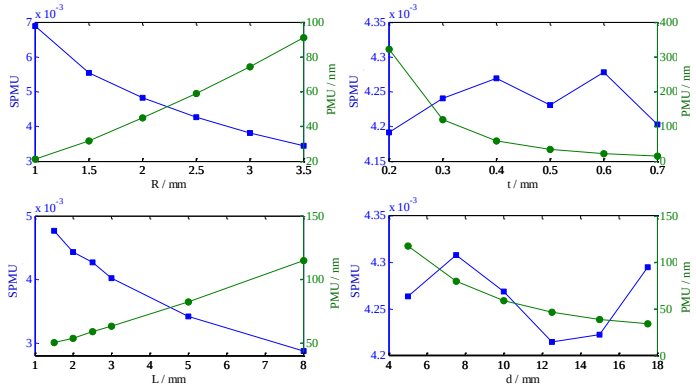

(a) Motions in the x-axis direction

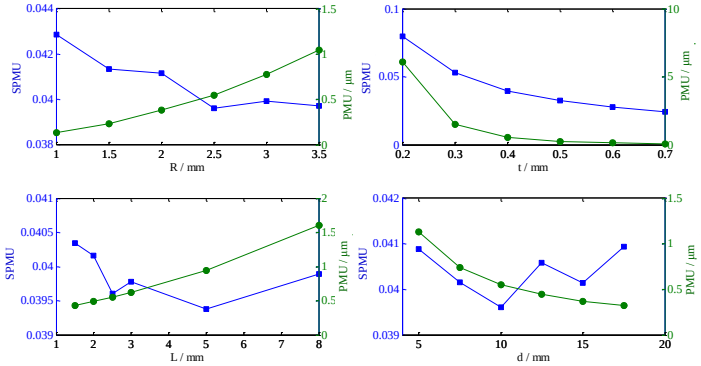

(b) Motions in the y-axis direction

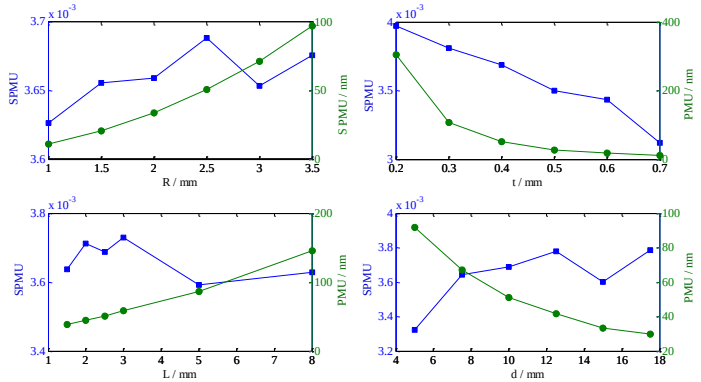

(c) Motions in the z-axis direction

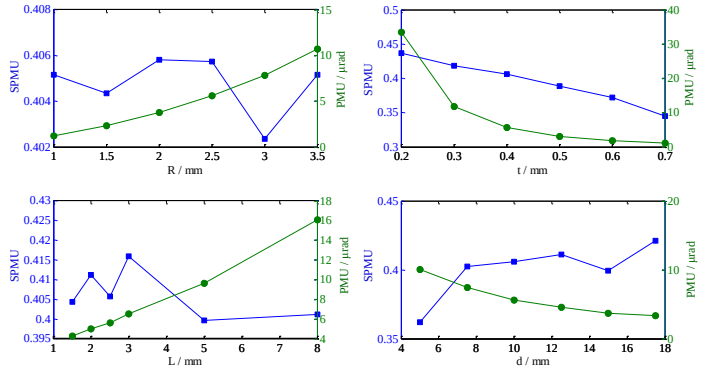

(d) Rotations around the x-axis

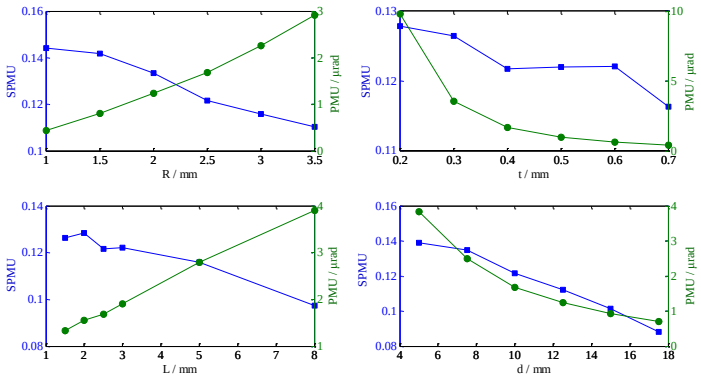

(e) Rotations around the y-axis

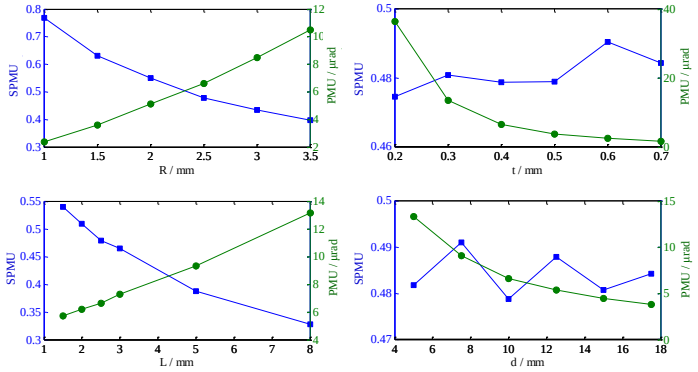

(f) Rotations around the z-axis

Fig. 6 Characteristics of spatial parasitic motions, where the lines with circle marks and rectangle marks correspond to the PMU and the SPMU, respectively

The results in Fig 6 show that the PMU in the *y*-axis direction may range from several hundred nanometers to several micrometers. It is about an order larger than the PMUs in both the *x*-axis and the *z*-axis directions. The three rotational PMUs remain in the same level, which may range within several dozens of micro-radians. Generally, it is in the rotation resolution level of typical rotational mechanisms. Although the values of the rotational PMUs are small, the derived Abbe errors cannot be ignored when considering the rotational length induced amplification effects. Considering the requirements and the working conditions of this sort of mechanism, the PMUs are relatively large and may significantly deteriorate working performances of the constructed mechatronic systems.

Furthermore, the PMUs in all the six directions will exponentially increase with the increase of the radius of the RCFH (*R*), while an approximately linear increase will occur with the increase of the parameter *L*. In contrast, with the increases of the parameters *t* and *d*, nearly exponential decreases of the PMUs can be observed. On the other hand, the mean vales of the parasitic motions are approximately zero except the motions in the *y*-axis direction. The skewness and the kurtosis obtained in each

simulation are around zero and present no dependency on the four structure parameters. It suggests that the parasitic motions well obey the Gaussian distribution law.

In view of the SPMUs of the translation motions, the SPMU in the *y*-axis direction caused by the structure distortions is more significant (~5%), which is about an order larger than that in both the *x*-axis and the *z*-axis directions (~0.4%). The SPMU in the *y*-direction will exponentially decrease with the increase of the parameter *t*, while there appears to be no obvious dependency on the parameters *R*, *L* and *d*. The slight fluctuations of the sensitivities are caused by the statistic essence of the simulation processes. Similarly, the SPMU in the *x*-axis direction will exponentially decrease with the increase of the parameters *R* and *L*, while it shows no dependency on the variations of the parameters *t* and *d*. In addition, the SPMU in the *z*-axis direction has no relationships with the parameters *R* and *L*. It will gradually decrease with the increase of *t*, while increase with the decrease of *d*.

As for the rotational SPMUs, the SPMUs around the *y*-axis possess the lowest sensitivities to the variations of the structure parameters, and they will slightly decrease with the increases of the four parameters *R*, *t*, *L* and *d*. The SPMU around the *x*-axis will linearly decrease with the increase of the parameter *t*, while it will slightly increase with the increase of the parameter *d*. As for the SPMU around the *z*-axis, it will exponentially decrease with the increase of *R* and *L*, while showing no dependence on parameters *t* and *d*.

3.3.2 Effects of manufacturing uncertainty

Generally, there are two sets of manufacturing uncertainties, one set is described by the position uncertainties (δR_i, δx_i and δb), and the other set is described by angle

uncertainties ($\alpha_{U,}$ α_L, and ϕ_i). To reveal the dependences of the PMUs on the manufacturing uncertainties, the Monte Carlo simulations are also conducted here with respect to different manufacturing uncertainties. When investigating the position uncertainties, the angles uncertainties are set the same as the ones in the last section, resulting in the relationships shown in Fig. 7. Since the translational SPMUs in the *z* direction and the rotational SPMUs around the *x*-axis and the *y*-axis remain unchanged, only the three other terms are presented. Similarly, when investigating the angle uncertainties, the position uncertainties are set the same as the ones in the last section. The results are illustrated in Fig. 8.

Figures 7 and 8 show that the SPMUs linearly increase with the increase of manufacturing uncertainties. As shown in Fig. 8, the SPMU in the *y*-axis direction possesses no dependency on the variations of the angle uncertainties. Besides, a range of 0.3^o angle uncertainty will cause 0.2% and 0.5% SPMUs in the *x*-axis and the *z*-axis directions, respectively. It suggests that the PMU in the *z*-axis direction is more sensitive to the angle uncertainties than that in the *x*-axis direction. Similarly, the SPMUs around the *y*-axis and the *z*-axis are approximately of the same level with respect to angle uncertainties, while they are much lower than that around the *x*-axis.

The results demonstrate a simple relationship between the SPMUs and manufacturing uncertainties. The positioning errors of the WEDM tool will only induce planar parasitic motions, while the straightness errors of the WEDM tool and the vertical errors in the clamping will contribute to the SPMUs in all directions except the translation in the *y*-axis direction. To achieve a more reliable working performance with low cost, the manufacturing tolerance should be kept relatively small.

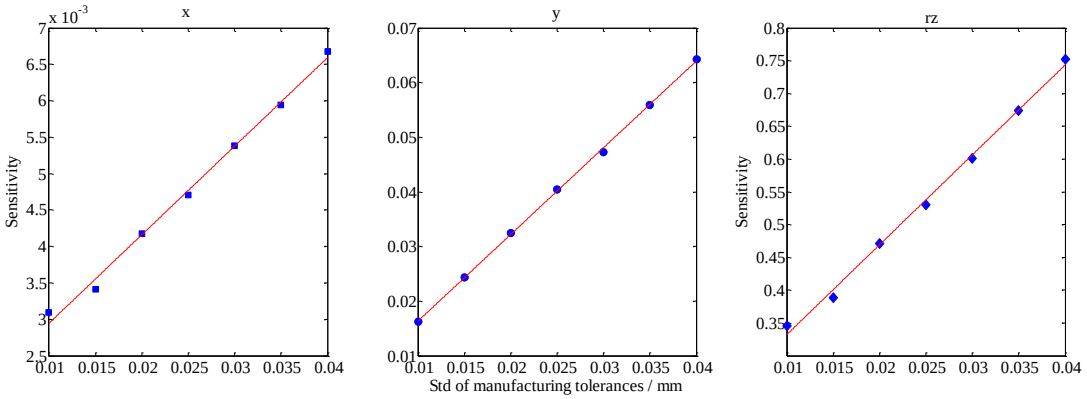

Fig. 7 SPMUs in terms of position uncertainties

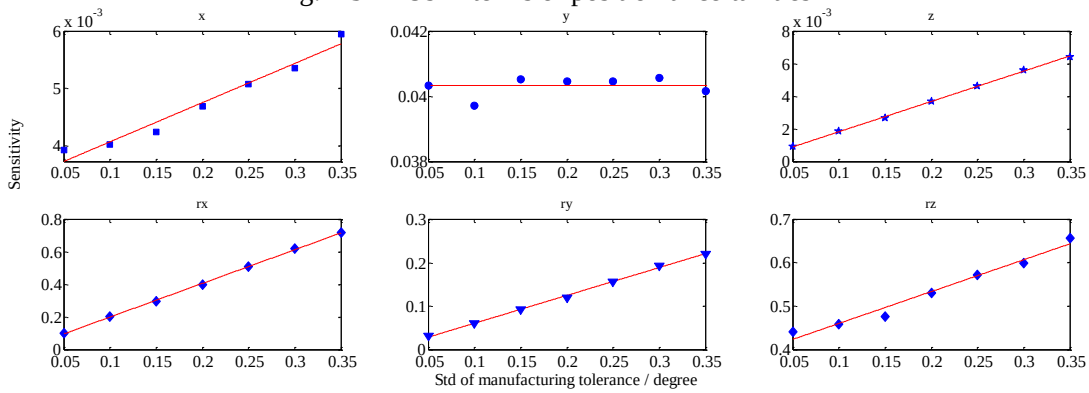

Fig. 8 SPMUs in terms of angle uncertainties

4. EXPERIMENTAL TESTS OF A TYPICAL DPCM

The authors of this paper previously designed a DPCM for micro-/nano machining with RCFHs in Ref. [38]. The parasitic motions of the mechanism in the *x*-axis and the *z*-axis directions are measured in this paper. To avoid introducing the profile of the reference surface into the measurement, the Renishaw X-80L laser interferometer is adopted for characterization, rather than laser or capacity based displacement measurement methods. A capacity transducer (Micro-sense II 5300) is employed for obtaining the output displacements of the mechanism in the working direction (*y*-axis). The photography of experiment setup is shown in Fig. 9. Note that two sets of Renishaw mirrors are used for measuring the parasitic motions in the two directions but only one set is illustrated in Fig. 9 to avoid repetition. During the measurement, the environment

compensation module Renishaw XC80 is adopted to compensate for the temperature, the air pressure and the humidity variations. To reduce external disturbances, the mechanism is installed on a vibration-isolated air-bearing platform Newport RS4000 with a RMS noise less than 5nm.

Parasitic motions in the *x*-axis and the *z*-axis directions are illustrated in Figs. 10(a) and 10(b) respectively. The measured parasitic motion in the *x*-axis direction is mainly caused by the corresponding translation errors and the yaw error. As shown in Fig. 9a, within a moving range of 116μm, the resulted parasitic motion in the *x*-axis direction is about 1.5 μm, showing a good linearity with respect to the working motion in the *y* direction. From the fitting results shown in Fig. 10(a), the moving error is about 14.7 nm per micrometer. The straightness error of the DPCM is extremely large when compared with some popular lubricated guides used in precision fields.

As for the parasitic motion in the *z*-axis direction shown in Fig. 10(b), an approximately quadratic relationship between the parasitic motion and the working motion is observed. The maximum deviation is about 3.12 μm whereas the motion in the working direction is about 86 μm. The measured parasitic motion in the *z*-axis direction is mainly caused by the translation in the *z*-axis direction and the pitch error. Since the measured result is the motion of the linear interferometer (part 2 in Fig. 9), the position variation along the *z*-axis can be determined by:

$$\chi = L_1 \sin(k^{\theta}\vartheta) + L_2 \cos(k^{\theta}\vartheta) + k^{\delta}\vartheta \tag{16}$$

where k^{δ} and k^{θ} denote the proportionality coefficients of the translation errors and pitch errors with respect to the working motion ϑ, L_1 and L_2 are the distances from the output end to the pitch axis and the interferometer, respectively.

From the relationship expressed in Eq. 16, it can be seen that the result obtained in Fig. 10(b) is essentially a harmonic curve, and details of the parasitic motion are determined by the parameters shown in Eq. 16. However, it is hard to identify the pitch angle error, the translation error and the center of the pitch motion. Thus, only the hybrid parasitic motion is presented here to characterize MESPM in the *z*-axis direction.

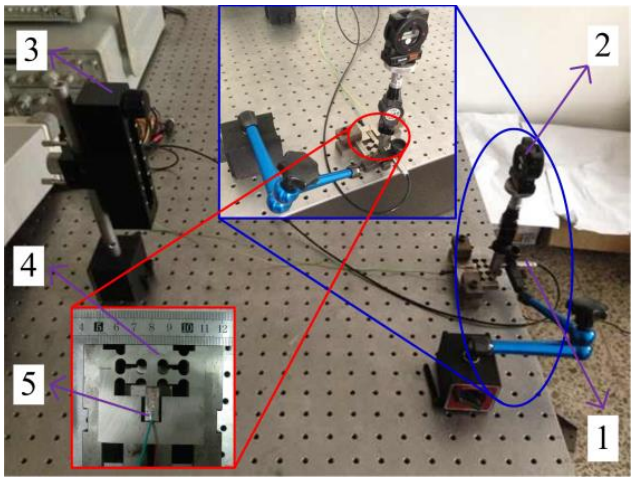

Fig. 9 Experimental setup for measuring parasitic motions (1. Capacitive displacement sensor; 2. Linear interferometer; 3. Reflector; 4. The DPCM; 5. Piezoelectric actuator)

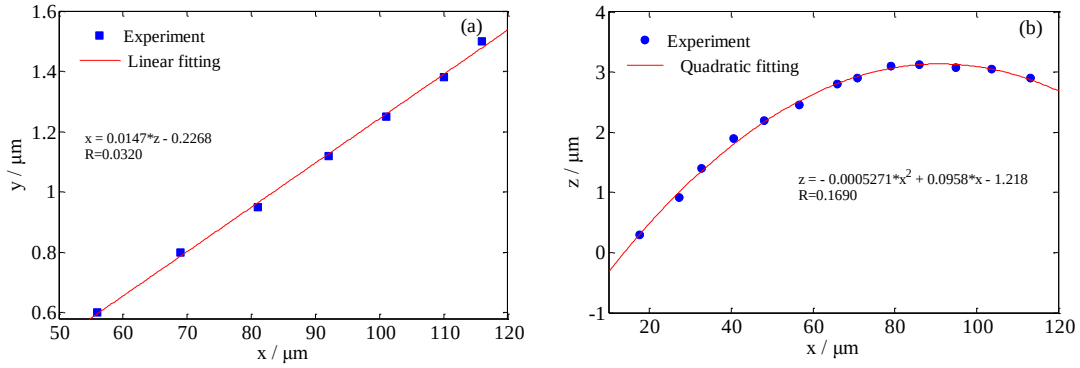

Fig. 10 Parasitic motions of the mechanism in (a) the *x*-axis direction and (b) the *z*-axis direction

5. CONCLUSIONS

Manufacturing error induced spatial parasitic motions (MESPM) of compliant mechanisms are comprehensively discussed from a statistical point of view. The complete compliance matrix of an imperfect flexural linkage (IFL), which is a basic element of a wide spectrum of compliant mechanisms, is theoretically derived. Based on the established elastic deformation model of the IFL, a case study of a well-known double parallelogram compliant mechanism with manufacturing errors is conducted. The main conclusions of this paper can be summarized as follows.

(a) Geometric features of the IFL with structural distortion are analytically characterized, and the elastic deformation behavior is accordingly modeled by applying the novel finite beam based matrix modeling (FBMM) method. Good agreements between the analytical and the finite element analysis (FEA) results clearly demonstrate the effectiveness of the FBMM method for describing the IFL.

(b) The Monte Carlo simulation is conducted to investigate the statistical behavior of MESPM. The spatial parasitic motions nearly follow perfect Gaussian distributions with respect to the Gaussian distributions of the manufacturing uncertainties. The sensitivity of the parasitic motion uncertainty is defined, and the dependence of the sensitivity to structure parameters and manufacturing uncertainties is discussed. Following the proposed analysis method, the structure parameters and the manufacturing tolerances can be optimally determined for a specified compliant mechanism.

(c) The parasitic motions of a typical DPCM in the *x*-axis and *z*-axis directions are experimentally characterized by the laser interferometer based measurement. The obtained parasitic motion in the *x*-axis direction is about 14.7 nm per micrometer, showing a linear relationship with the working motion. Also, an essential harmonic

relationship between the parasitic motion in the *z*-axis direction and the working motion is obtained, and the obtained maximum deviation is about 3.12μm with respect to a working stroke of 120μm.

ACKNOWLEDGMENT

The work described in this paper was supported by the Research Committee of The Hong Kong Polytechnic University (RTJZ) and the National Science Foundation of China (51275434, 51175221).

REFERENCES

[1] Tian, Y., Shirinzadeh, B., and Zhang, D., 2009, "A Flexure-Based Mechanism and Control Methodology for Ultra-Precision Turning Operation," Precision Engineering, 33(2), pp. 160-166. DOI: 10.1016/j.precisioneng.2008.05.001

[2] Li, Y., and Xu, Q., 2009, "Design and Analysis of a Totally Decoupled Flexure-Based XY Parallel Micromanipulator," Robotics, IEEE Transactions on, 25(3), pp. 645-657. DOI: 10.1109/TRO.2009.2014130

[3] Yong, Y., Moheimani, S., Kenton, B. J., and Leang, K., 2012, "Invited Review Article: High-Speed Flexure-Guided Nanopositioning: Mechanical Design and Control Issues," Review of Scientific Instruments, 83(12), pp. 121101. DOI: 10.1063/1.4765048

[4] Huang, H., Zhao, H., Mi, J., Yang, J., Wan, S., Yang, Z., Yan, J., Ma, Z., and Geng, C., 2011, "Experimental Research on a Modular Miniaturization Nanoindentation Device," Review of Scientific Instruments, 82(9), pp. 095101. DOI: 10.1063/1.3632980

[5] Marinello, F., Carmignato, S., Voltan, A., De Chiffre, L., and Savio, E., 2010, "Error Sources in Atomic Force Microscopy for Dimensional Measurements: Taxonomy and Modeling," Journal of Manufacturing Science and Engineering, 132(3), pp. 030903. doi:10.1115/1.4001242

[6] Kashani, M. S., and Madhavan, V., 2011, "Analysis and Correction of the Effect of Sample Tilt on Results of Nanoindentation," Acta Materialia, 59(3), pp. 883-895. DOI: 10.1016/j.actamat.2010.09.051

[7] Huang, H., Zhao, H., Shi, C., and Zhang, L., 2013, "Using Residual Indent Morphology to Measure the Tilt between the Triangular Pyramid Indenter and the

Sample Surface," Measurement Science and Technology, 24(10), pp. 105602. DOI:10.1088/0957-0233/24/10/105602

[8] Huang, L., Meyer, C., and Prater, C., 2007, "Eliminating Lateral Forces During AFM Indentation," Journal of Physics: Conference Series, 61, pp. 805. DOI:10.1088/1742-6596/61/1/161

[9] Ren, J., and Zou, Q., 2014, "A Control-Based Approach to Accurate Nanoindentation Quantification in Broadband Nanomechanical Measurement Using Scanning Probe Microscope," Nanotechnology, IEEE Transactions on 13(1), pp. 46-54. DOI: 10.1109/TNANO.2013.2287505

[10] Kim, J. H., Kim, S. H., and Kwak, Y. K., 2004, " ," Sensors and Actuators A: Physical, 116(3), pp. 530-538. DOI: 10.1016/j.sna.2004.05.027

[11] Hwang, D., Byun, J., Jeong, J., and Lee, M. G., 2011, "Robust Design and Performance Verification of an in-Plane XYθ Micro-positioning Stage," Nanotechnology, IEEE Transactions on, 10(6), pp. 1412-1423. DOI: 10.1109/TNANO.2011.2159015

[12] Li, Y., and Xu, Q., 2009, "Modeling and Performance Evaluation of a Flexure-Based XY Parallel Micromanipulator," Mechanism and Machine Theory, 44(12), pp. 2127-2152. DOI: 10.1016/j.mechmachtheory.2009.06.002

[13] Polit, S., and Dong, J., 2011, "Development of a High-Bandwidth XY Nanopositioning Stage for High-Rate Micro-/Nanomanufacturing," Mechatronics, IEEE/ASME Transactions on, 16(4), pp. 724-733. DOI: 10.1109/TMECH.2010.2052107

[14] Dibiasio, C. M., and Hopkins, J. B., 2012, "Sensitivity of Freedom Spaces During Flexure Stage Design Via FACT," Precision Engineering, 36(3), pp. 494-499. DOI: 10.1016/j.precisioneng.2012.03.003

[15] Kang, D., and Gweon, D., 2013, "Analysis and Design of a Cartwheel-Type Flexure Hinge," Precision Engineering, 37(1), pp. 33-43. DOI: 10.1016/j.precisioneng.2012.06.005

[16] Niaritsiry, T.-F., Fazenda, N., and Clavel, R., 2004, "Study of the Sources of Inaccuracy of a 3 Dof Flexure Hinge-Based Parallel Manipulator," In: Proceedings of Robotics and Automation, 2004 IEEE International Conference on, 4, pp. 4091-4096. DOI: 10.1109/ROBOT.2004.1308911

[17] Patil, C. B., Sreenivasan, S., and Longoria, R. G., 2008, "Analytical and Experimental Characterization of Parasitic Motion in Flexure-Based Selectively Compliant Precision Mechanisms," In: ASME Proceedings of 32nd Annual Mechanisms and Robotics Conference, pp. 393-404. DOI:10.1115/DETC2008-50111

[18] Li, S., and Yu, J., 2014, "Design Principle of High-Precision Flexure Mechanisms Based on Parasitic-Motion Compensation," Chinese Journal of Mechanical Engineering, 27(4), pp. 663-672. DOI: 10.3901/CJME.2014.0415.076

[19] Smith, S., Chetwynd, D., and Bowen, D., 1987, "Design and Assessment of Monolithic High Precision Translation Mechanisms," Journal of Physics E: Scientific Instruments, 20(8), pp. 977.

[20] Hopkins, J. B., and Culpepper, M. L., 2010, "A Screw Theory Basis for Quantitative and Graphical Design Tools That Define Layout of Actuators to Minimize Parasitic Errors in Parallel Flexure Systems," Precision Engineering, 34(4), pp. 767-776. DOI: 10.1016/j.precisioneng.2010.05.004

[21] Patil, C. B., Sreenivasan, S., and Longoria, R. G., 2008, "Robust Design of Flexure Based Nano Precision Compliant Mechanisms with Application to Nano Imprint Lithography," In: ASME Proceedings of 2nd International Conference on Micro- and Nanosystems (MNS), pp. 701-711. DOI:10.1115/DETC2008-50114

[22] Patil, C. B., Sreenivasan, S., and Longoria, R. G., 2007, "Analytical Representation of Nano-Scale Parasitic Motion in Flexure-Based One Dof Translation Mechanism," In: ASPE 22nd Annual Meeting.

[23] Ryu, J. W., and Gweon, D.-G., 1997, "Error Analysis of a Flexure Hinge Mechanism Induced by Machining Imperfection," Precision Engineering, 21(2), pp. 83-89. DOI: 10.1016/S0141-6359(97)00059-7

[24] Huh, J., Kim, K., Kang, D., Gweon, D., and Kwak, B., 2006, "Performance Evaluation of Precision Nanopositioning Devices Caused by Uncertainties Due to Tolerances Using Function Approximation Moment Method," Review of scientific instruments, 77(1), pp. 015103. DOI: 10.1063/1.2162750

[25] Valentini, P. P., and Hashemi-Dehkordi, S.-M., 2013, "Effects of Dimensional Errors on Compliant Mechanisms Performance by Using Dynamic Splines," Mechanism and Machine Theory, 70, pp. 106-115. DOI: 10.1016/j.mechmachtheory.2013.07.007

[26] Lobontiu, N., Paine, J. S., Garcia, E., and Goldfarb, M., 2001, "Corner-Filleted Flexure Hinges," Journal of Mechanical Design, 123(3), pp. 346-352. DOI: 10.1115/1.1372190

[27] Chen, G., Liu, X., and Du, Y., 2011, "Elliptical-Arc-Fillet Flexure Hinges: Toward a Generalized Model for Commonly Used Flexure Hinges," Journal of Mechanical Design, 133(8), pp. 081002. DOI: 10.1115/1.4004441

[28] Tian, Y., Shirinzadeh, B., and Zhang, D., 2010, "Closed-Form Compliance Equations of Filleted V-Shaped Flexure Hinges for Compliant Mechanism Design," Precision Engineering, 34(3), pp. 408-418. DOI: 10.1016/j.precisioneng.2009.10.002

[29] Zhu, Z., Zhou, X., Wang, R., and Liu, Q., 2015, "A Simple Compliance Modeling Method for Flexure Hinges," Science China Technological Sciences, 58(1), pp. 56-63. DOI: 10.1007/s11431-014-5667-1

[30] Wang, R., Zhou, X., and Zhu, Z., 2013, "Development of a Novel Sort of Exponent-Sine-Shaped Flexure Hinges," Review of Scientific Instruments, 84(9), pp. 095008. DOI: 10.1063/1.4821940

[31] Cowper, G., 1966, "The Shear Coefficient in Timoshenko's Beam Theory," Journal of applied mechanics, 33, pp. 335-340. DOI:10.1115/1.3625046

[32] Chen, G., and Howell, L. L., 2009, "Two General Solutions of Torsional Compliance for Variable Rectangular Cross-Section Hinges in Compliant Mechanisms," Precision Engineering, 33(3), pp. 268-274. DOI: 10.1016/j.precisioneng.2008.08.001

[33] Zhu, Z., Zhou, X., Liu, Z., Wang, R., and Zhu, L., 2014, "Development of a Piezoelectrically Actuated Two-Degree-of-Freedom Fast Tool Servo with Decoupled Motions for Micro-/Nanomachining," Precision Engineering, 38(4), pp. 809–820. DOI: 10.1016/j.precisioneng.2014.04.009

[34] Koseki, Y., Tanikawa, T., Koyachi, N., and Arai, T., 2000, "Kinematic Analysis of Translational 3-Dof Micro Parallel Mechanism Using Matrix Method," In: Proceedings of Intelligent Robots and Systems, IEEE/RSJ International Conference on, 1, pp. 786-792. DOI: 10.1109/IROS.2000.894700

[35] Tang, H., and Li, Y., 2013, "Design, Analysis, and Test of a Novel 2-Dof Nanopositioning System Driven by Dual Mode," IEEE Transactions on Robotics, 29(3), pp. 650-662. DOI: 10.1109/TRO.2013.2248536

[36] Meijaard, J., 2011, "Refinements of Classical Beam Theory for Beams with a Large Aspect Ratio of Their Cross-Sections," In: IUTAM Symposium on Dynamics Modeling and Interaction Control in Virtual and Real Environments, pp. 285-292. DOI: 10.1007/978-94-007-1643-8_32

[37] Brouwer, D., Meijaard, J., and Jonker, J., 2013, "Large Deflection Stiffness Analysis of Parallel Prismatic Leaf-Spring Flexures," Precision engineering, 37(3), pp. 505-521. DOI: 10.1016/j.precisioneng.2012.11.008

[38] Zhu, Z., Zhou, X., Liu, Q., and Zhao, S., 2011, "Multi-Objective Optimum Design of Fast Tool Servo Based on Improved Differential Evolution Algorithm," Journal of mechanical science and technology, 25(12), pp. 3141-3149. DOI: 10.1007/s12206-011-0824-y

Figure Captions List

Fig. 1 Schematic of a typical flexural linkage

Fig. 2 Structure characteristic of the IFL

Fig. 3 Schematic of the linkages derived from the mathematical model

Fig. 4 A typical DPCM

Fig. 5 Variations of the std of deformations in the y-axis direction

Fig. 6 Fig. 5 Characteristics of spatial parasitic motions, where the lines with circle marks and rectangle marks correspond to the PMU and the SPMU, respectively. (a) Motions in the x-axis direction; (b) Motions in the y-axis direction; (c) Motions in the z-axis direction; (d) Rotations around the x-axis; (e) Rotations around the y-axis; (f) Rotations around the z-axis;

Fig. 7 SPMUs in terms of position uncertainties

Fig. 8 SPMUs in terms of angle uncertainties

Fig. 9 Experimental setup for measuring parasitic motions (1. Capacitive displacement sensor; 2. Linear interferometer; 3. Reflector; 4. The DPCM; 5. Piezoelectric actuator).

Fig. 10 Parasitic motions of the mechanism in (a) the x-axis direction and (b) the z-axis direction

Table Caption List